Graphene *in* Composite Materials

Synthesis, Characterization and Applications

Nikhil A. Koratkar, Ph.D.

*John A. Clark and Edward T. Crossan Chair
Professor, Mechanical, Aerospace and Nuclear Engineering
and Materials Science and Engineering
Rensselaer Polytechnic Institute*

DES*tech* Publications, Inc.

Graphene in Composite Materials

Preface

SINCE its rise to prominence in 2004, graphene has captivated the attention of the worldwide scientific community, including academia, government, and industry. Perhaps no other material has had such an impact in such a short period of time. The remarkable blend of mechanical, electrical, thermal, optical, and wetting properties of graphene stem from its unique two-dimensional single-carbon-atom-thick hexagonal honeycomb lattice. Graphene is the thinnest, stiffest, and strongest material known to humankind and is also an excellent conductor of both heat and electricity. It is an ideal impermeable membrane that can passivate surfaces onto which it is coated. The basal plane of graphene is also extremely inert and highly resistant to oxidation. In many of these qualities, graphene bears a resemblance to carbon nanotubes. However, there are two important differences. First, graphene is two-dimensional, so it is far easier to work with compared to one-dimensional nanotubes and nanowires. It is much simpler to manipulate graphene on surfaces and to contact them electrically for various device applications. Second, carbon nanotubes do not exist in nature, while graphene is available in bulk graphite. This means that, while carbon nanotubes have to be assembled atom-by-atom using tedious, time-consuming, and expensive bottom-up synthesis techniques, graphene can be produced in bulk using relatively inexpensive and scalable top-down synthesis methods, such as exfoliation of graphite oxide or other graphite intercalation compounds. This potentially gives graphene a tremendous advantage over other forms of nanomaterials in terms of its cost-effectiveness for commercial applications.

The 2010 Nobel Prize in Physics awarded to Andre Geim and Kon-

stantin Novoselov of the University of Manchester, UK, has directed great attention towards graphene and its potential applications. In my view, the most promising and technically feasible application of graphene for near-term practical implementation is as a nanofiller in composites. This includes polymer, ceramic, as well as metal matrix composite materials. Such materials are the basic building blocks of most engineering systems and devices. Graphene shows enormous potential to improve the mechanical, thermal, and electrical properties of such composites at ultra-low nanofiller loading fractions. This, coupled with the cost-effectiveness of graphene production (i.e., via top-down exfoliation of graphite), could result in the next generation of composite materials. These materials could find a myriad of applications, from lightweight aerospace structures used in aircraft, rotorcraft, and spacecraft, to adhesives, paints, thermal interface materials, wear- and scratch-resistant coatings, and construction materials for automobiles, boats, and building applications. The sky is the limit for such advanced composite materials and the possible uses of such technologies are only limited by our imagination.

This book is aimed at introducing graphene composites to engineering graduate and undergraduate students and academics, as well as industry and government researchers. The book is essentially a compilation of over a dozen research papers published by my group at the Rensselaer Polytechnic Institute over the last several years on this topic. The essential elements of these papers, along with other relevant work performed by other research groups, have been distilled and organized in this book into five chapters. I have attempted to simplify the language and explanation of the materials so readers who may possess only a rudimentary knowledge of graphene and its composites can easily comprehend it. The first chapter introduces the reader to the history of graphene, its place among the family of carbon allotropes, its properties, its synthesis, and its characterization methods. Chapter 2 is the main focus of this book and describes how graphene platelets and graphene nanoribbons can be infiltrated into bulk polymer systems to improve their mechanical, thermal, and electrical properties. The mechanical properties considered include Young's Modulus, ultimate tensile strength, viscoelastic properties, bucking resistance, creep response, and wear resistance, as well as basic fracture mechanics properties such as fracture toughness and fatigue resistance. The thermal conductivity and electrical conductivity enhancements induced by formation of graphene percolation networks in polymers are also considered in Chapter 2. In many realistic applications, microfibers are necessary

to carry the load and, hence, Chapter 3 discusses how graphene-infused epoxy resins can be paired with conventional carbon, glass, or Kevlar fibers to create unique hierarchically organized composites. In particular, the fatigue life properties of such hierarchical materials show dramatic improvements when compared with traditional fiber-reinforced composites. In Chapter 4, I discuss the possibilities for extending the application of graphene beyond polymer systems to include ceramic, as well as metal-matrix composites. Chapter 5 describes an unconventional type of graphene composite–namely nanofluids with a fluid serving as the liquid matrix. Such graphene colloidal dispersions can be stable for extended periods of time and could find a wide range of possible applications, from cutting fluids and coolants, to coatings with controllable wetting properties, to nanofuels for enhanced combustion.

My intention is to provide the reader with a broad perspective of the possibilities and the limitations of graphene-based composite materials. The field is still young and is rapidly evolving. Thousands of researchers worldwide are engaged in graphene composites research and are constantly pushing the boundaries of what is known regarding graphene and its composites. My hope is that this book will benefit the graphene research community and industry. This book would not have been possible without the efforts of my dedicated Ph.D. students (both past and present). I have been truly blessed to have had the opportunity to work with such an energetic, ambitious, and talented group of students. In particular, I would like to thank Mohammad Ali Rafiee, Fazel Yavari, Iti Srivastava, Ardavan Zandiatashbar, Javad Rafiee, Prashant Dhiman, Abhay Thomas, Rahul Mukherjee, Ajay Krishnamurthy, Eklavya Singh, and Jing Zhong. Special thanks also to my faculty collaborators including Professor Zhong-Zhen Yu (Beijing Institute of Chemical Technology, China), Professor Pulickel Ajayan and Professor James Tour (Rice University, USA), Dr. Stephen Bartolucci (US Army Benet Labs, USA), Professor Erica Corral (University of Arizona, USA), and my colleagues Professor Theodorian Borca Tasciuc, Professor Catalin Picu, Professor Linda Schadler, and Professor Yunfeng Shi (at Rensselaer Polytechnic Institute, USA). I am deeply indebted to these individuals for many stimulating discussions and for sharing their knowledge, wisdom, and insight with me. Finally, I would like to express my deep love and gratitude to my family—specifically, my mother (Nirmala), father (Ashok), wife (Rashmi), and children (Mihir and Savani). Your patience, support, encouragement, and sacrifices have enabled me to pursue my dreams in an unfettered manner and I dedicate this book to all of you.

Introduction to Graphene

BEFORE delving into the topic of graphene-based composite materials, it is essential to understand the structure/properties of graphene and graphene's place in the family of nanocarbon materials. The intent of this chapter is to provide the reader with a general introduction to the various allotropes of carbon that range from the well-known diamond and graphite, to newly discovered nanocarbons such as fullerenes, single-walled carbon nanotubes, multi-walled carbon nanotubes, and graphene. Graphene is, in fact, the basic building block of all forms of sp^2 hybridized carbon materials and is, therefore, of great interest both from the scientific and technological standpoint. This chapter discusses the structure of graphene and some of its key mechanical, electrical, thermal, and optical properties. It addresses the synthesis of graphene, considering both top-down and bottom-up methods for its production. This is followed by graphene characterization methods, including both microscopy- and spectroscopy-based techniques. Finally, this chapter covers why graphene is particularly promising as a nanofiller in composite materials. This lays the foundation for the subsequent chapters of this book, which cover various aspects of graphene-based composite materials.

The bulk of the material included in this chapter has been adapted from References [1–69], published by the author's group, his collaborators and other researchers.

1.1. ALLOTROPES OF CARBON

1.1.1. Diamond and Graphite

The electronic structure of carbon gives rise to its ability to bond in

many different configurations and form structures with distinctly differ-ent characteristics. This is clearly manifested in diamond and graphite [1], which are the two most commonly observed forms of carbon. Dia-mond forms when the four valence electrons in a carbon atom are sp3 hy-bridized (i.e., all bonds shared equally to four neighboring atoms), which results in a three-dimensional (3D) diamond cubic structure. Diamond is the hardest material known to humankind due to this 3D network of carbon-carbon (C–C) bonds. It is also special in that it is one of the very few materials in nature that is both electrically insulating and thermally conductive. On the other hand, graphite is the sp^2 hybridized form of carbon and contains only three bonds per carbon atom. The fourth va-lence electron is in a delocalized state, and is consequently free to float or drift among the atoms, since it is not bound to one particular atom in the structure. This creates a planar hexagonal structure (called graphene) and gives rise to the layered structure of graphite that is composed of stacked two-dimensional (2D) graphene sheets. Graphite contains strong cova-lent bonds between the carbon atoms within individual graphene sheets, which gives rise to its outstanding in-plane mechanical properties. How-ever, the van der Waal's forces between adjacent graphene sheets in the layered structure are relatively weak and, therefore, graphite is much soft-er than diamond. Similar to diamond, graphite (in-plane) is a good con-ductor of heat; however, the free electrons present in graphite also endow it with high in-plane electrical conductivity, unlike diamond. The structure of diamond and graphite are depicted schematically in Figure 1.1.


(a)   (b)
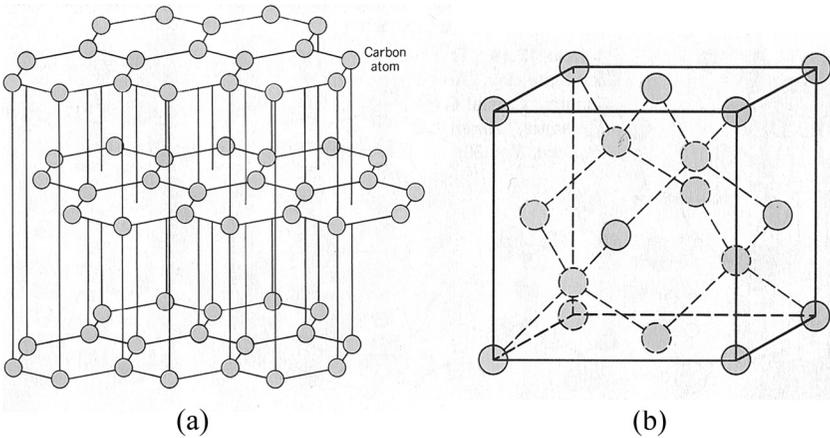
FIGURE 1.1. *Schematic of the atomic structure for (a) graphite, showing the sp^2 hybrid-ized hexagonal lattice, and (b) sp^3 hybridized diamond, which consists of the 3-dimen-sional diamond cubic lattice. (Adapted from [1] with permission).*

1.1.2. Fullerenes and Carbon Nanotubes

In the last three decades, various exotic forms of nanocarbon materials have been discovered and this has revolutionized carbon science. Before the advent of graphene, fullerenes and carbon nanotubes were the most well-known nanocarbon allotropes. Both of these materials utilize the sp^2 hybridization of carbon to create self-contained molecules containing several tens or hundreds of carbon atoms. Richard Smalley and Harold Kroto first discovered fullerenes [2] in the mid-1980s. The most common of these molecules, C_{60}, has the structure of a soccer ball, containing 20 hexagon and 12 pentagon faces, with carbon atoms at each vertex. This structure is shown in Figure 1.2(a) and compared to amorphous carbon [Figure 1.2(b)], which is yet another carbon allotrope. It has been shown that pentagonal defects create a curvature in the 2D graphene structure and, with six pentagons, a complete hemisphere of a fullerene is created. Thus, 12 pentagons are necessary to form a fullerene structure. Such closed nanocarbon structures appear to be stable due to the high energy of dangling bonds at the edges of nanosized graphene sheets. Because the free energy decrease due to satisfying these bonds is larger than the increase in bond energy by distorting the C–C bond length and angles, enclosed graphitic carbon structures such as fullerenes are created.

It can be conceived that by adding atoms to the basic structure of a fullerene, larger spherical or oblong structures are possible. In 1991, Sumio Iijima [3] discovered the carbon nanotube (CNT), the most prominent of these novel carbon materials. A single-walled carbon nanotube (SWNT) can be simply considered as a graphene sheet that has been rolled up seamlessly into a tube, and capped at the end with six pentagonal defects, as in fullerenes. By changing the way the graphene sheet is rolled into a tube [3–6], SWNT can be formed with different diameters and chiralities (or helicities). Each nanotube is characterized by a helical angle, or a chiral vector, which represents this direction of rolling. Two unique SWNT types are the zig-zag tube, which is characterized by a chiral vector of (n,0) and has C–C bonds oriented perpendicular to the tube axis; and an armchair tube, which has a chiral vector of (n,n), and C–C bonds parallel to the tube axis. Figure 1.3(a)–(c) provide schematic examples of an armchair, a zig-zag, and a randomly oriented SWNT. Multi-walled carbon nanotubes (MWNTs) consist of a number of concentric SWNT cylinders, which share a common axis. The inter-shell spacing in MWNTs is ~3.4 Å, slightly larger than

(a)   (b)
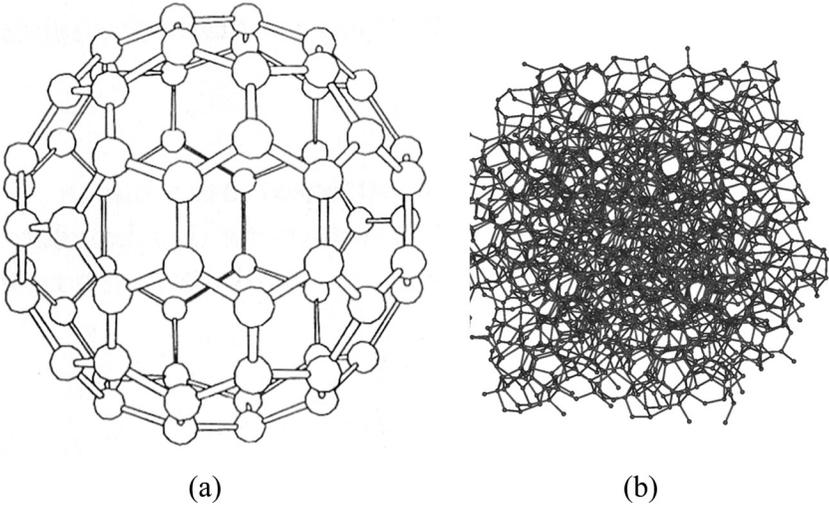
FIGURE 1.2. *(a) Soccer ball-like shape of a C_{60} fullerene molecule showing the hexagonal graphite-like lattice with pentagon defects closing the spherical shell structure. (b) Molecular model of an amorphous carbon cluster. (Adapted from [4] with permission).*


(a)

(b)

(c)
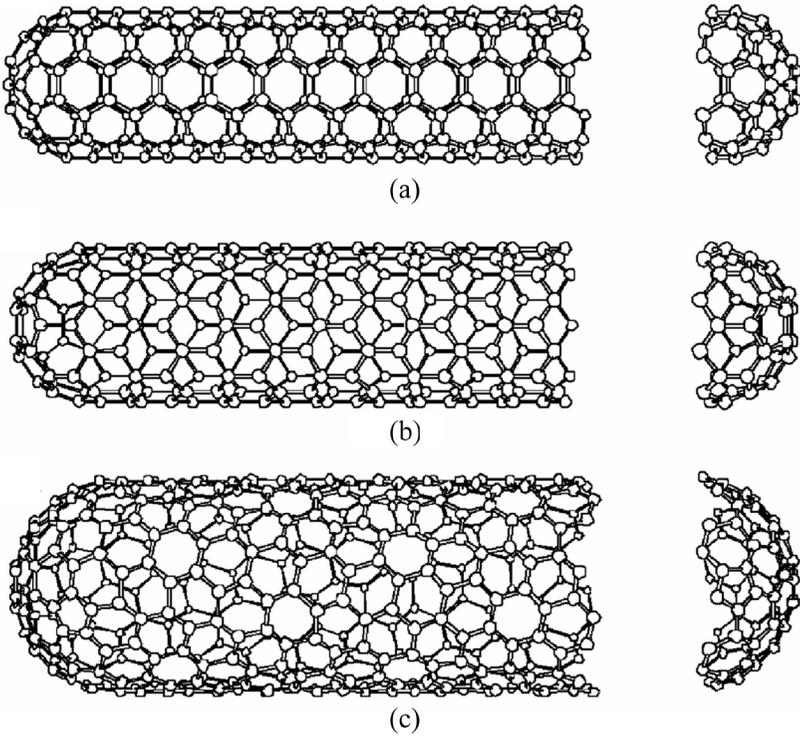
FIGURE 1.3. *Model of three possible single-walled nanotubes; (a) (5,5) armchair nanotube, (b) (9,0) zig-zag nanotube, and (c) randomly oriented (10,5) nanotube. (Adapted from [6] with permission).*

4

that of graphite, which has an ideal inter-plane spacing of ~3.35 Å [6]. Typical SWNT diameters lie in the 1–2 nanometer (nm) range, while MWNTs are relatively larger with diameters in the 20–40 nm range. The lengths of SWNT and MWNT can be as large as several hundred microns, thus carbon nanotubes constitute ideal one-dimensional (1D) structures. SWNT can be either semi-conducting or metallic, depending on their chiral vector, while MWNT are typically always metallic in nature. Fullerenes and carbon nanotubes can be produced by laser ablation of a carbon source. Carbon nanotubes can also be produced by arc-discharge and chemical vapor deposition processes.

1.1.3. Graphene

Graphene is a single-atom-thick sheet of sp^2 hybridized carbon atoms, which are packed in a hexagonal honeycomb crystalline structure [7–14]. Graphene is the thinnest material known to humankind; the atomic diameter of a carbon atom is ~0.14 nm. The in-plane dimensions of a graphene sheet can be several cm in size and, hence, it represents the ideal 2D sheet structure. Graphene is the fundamental building block of all sp^2 carbon materials including SWNTs, MWNTs, and graphite and is, therefore, interesting from a fundamental standpoint, as well as for practical applications. It was long believed that while graphene can be deposited on substrates (for example, using epi-


(a)   (b)
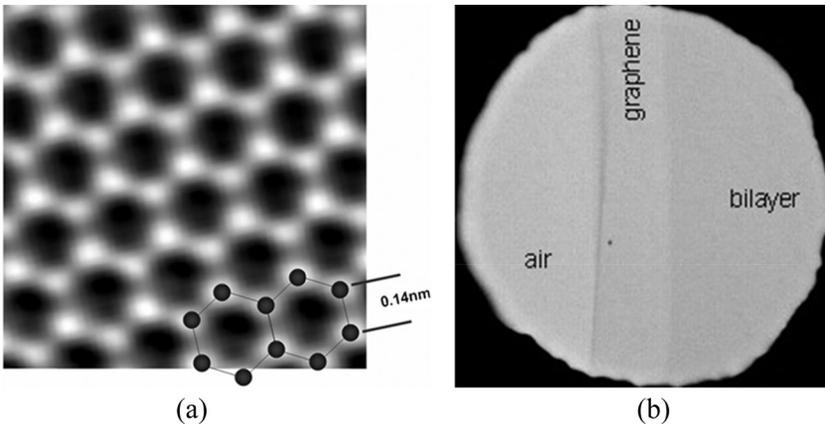
FIGURE 1.4. (a) Transmission electron microscopy image of graphene illustrating the crystalline lattice (bond length ~0.14 nm). (Adapted from [15] with permission). (b) On Si substrates with ~300 nm oxide layer, graphene layers can be discerned using an optical microscope. (Adapted from [16] with permission).

taxial growth techniques), a free-standing (non-supported) graphene sheet would be thermodynamically unstable due to the high energy of dangling bonds at the edges of the sheet. Pioneering research in 2004 by Geim and Novoselov (2010 Nobel Prize winners in Physics) of the University of Manchester led to the isolation of a single free-standing sheet of graphene [7]. Geim and Novoselov used Scotch tape to peel layers of a bulk graphite crystal. They repeated this process until they were able to isolate a graphene monolayer (Figure 1.4).

1.2. PROPERTIES OF GRAPHENE

As a result of its unique two-dimensional crystal structure and ultra-strong sp^2 carbon bonding network, graphene offers an exciting blend of mechanical, electrical, thermal, and optical properties that opens the door to a variety of possible applications. The elastic modulus of an individual graphene sheet is predicted [17] to be ~1 TPa (or 1000 GPa). This has been validated [18] by atomic force microscopy (AFM)-based indentation experiments performed on suspended graphene. The exceptionally high modulus of graphene, coupled with its low density (~1–2 g/cm^3), implies that the specific modulus (i.e., modulus normalized by density) of graphene far exceeds that of all other structural materials, including aluminum, titanium, or steel. In addition to its very large elastic modulus, graphene also displays a fracture strength of ~125 GPa [18], which is superior to most commonly used structural materials.

Graphene has a very interesting electronic band structure. It is a semi-metal with zero electronic band gap; the local density of states at the Fermi level is zero and conduction can only occur by the thermal excitation of electrons [9]. However, an energy gap can be engineered in graphene's band structure using a variety of methods. These methods are based on the breaking of graphene's lattice symmetry, such as defect generation [19], water adsorption [20], applied bias [21–23], and interaction with gases (e.g., nitrogen dioxide or ammonia) [24]. Other remarkable properties of graphene that have been reported [25] include exceptionally high values of its in-plane thermal conductivity (~5,000 W $m^{-1}K^{-1}$), charge carrier mobility (200,000 cm^2 V^{-1} s^{-1}), and specific surface area (2,630 m^2 g^{-1}), plus fascinating phenomena such as the quantum Hall effect, spin resolved quantum interference, ballistic electron transport, and bipolar super-current, to name a few. It should, however, be noted that the exceptional thermal and electronic properties of graphene listed above typically hold only for free-standing

or suspended graphene and degrade markedly when the graphene is supported on a substrate platform. The number of journal publications related to graphene has increased exponentially over the past decade and there is no doubt that graphene has captivated the attention of the worldwide scientific community.

Another key property of graphene that is particularly important for optoelectronic applications is its optical transparency [26–28]. The optical absorption of a single graphene layer is shown to be ~2.3% over the visible spectrum, which, combined with its high electrical conductivity [29–30], could lead to transparent conductive electrodes [31–34]. Such electrodes could prove to be a viable replacement for transparent indium tin oxide (ITO)-based electrodes. ITO is brittle and, therefore, cannot be used in flexible electronics. Graphene, on the other hand, offers extreme flexibility; for this reason, optically transparent and electrically conductive graphene films could replace ITO for the next generation of flexible and stretchable electronics. In addition to optical transparency, another fascinating property of graphene is its wetting transparency [35]. Monolayer graphene coatings do not significantly disrupt the intrinsic wetting behavior of surfaces for which surface-water interactions are dominated by van der Waals forces. Figure 1.5(a)–(b) show water contact angle measurements performed on copper substrates with different numbers of graphene layers in between. The contact angle of water is obtained by drawing a tangent to the water droplet as it meets the solid surface. For complete wetting, the contact angle is zero, since water spontaneously wets the surface to form a liquid film. By contrast, if water completely dewets the surface, it will form a ball that will make a point contact with the solid surface, resulting in a contact angle of 180 degrees. Generally, surfaces with water contact angle > 150 degrees are called super-hydrophobic and surfaces that display contact angle < 20 degrees are termed super-hydrophilic. Figure 1.5(b) indicates that monolayer graphene causes minimal disruption in the baseline copper contact angle. With increasing numbers of graphene layers, the contact angle of water on copper gradually transitions towards the bulk graphite value, which is reached for ~6 graphene layers. Similar response has also been observed on gold and silicon, but not on glass [35].

The wetting transparency of graphene films can be comprehended from continuum modeling using the effective interface potential approach [36–39]. The basic idea is to consider the solid-liquid interfacial energy $W(h)$, defined as the excess free energy per unit area it takes to bring two interfaces from infinity to a certain distance h. By this
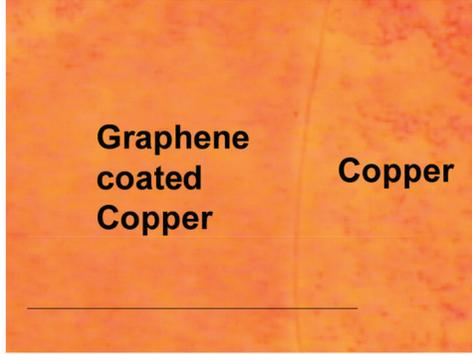
(a)
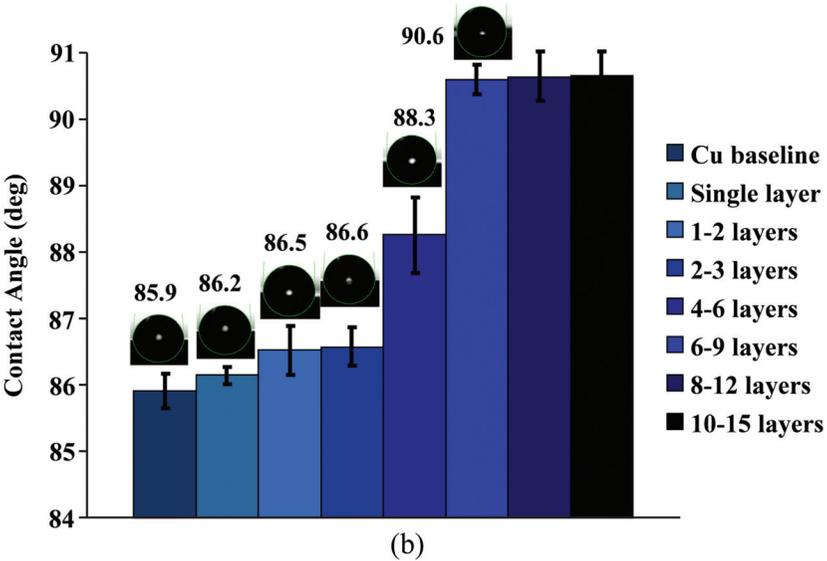
(b)

FIGURE 1.5. (a) Deposition of large area continuous graphene films on copper by chemical vapor deposition. (b) Water contact angle measurements on copper with different number of graphene layers placed on copper. (Adapted from [35] with permission).

definition, W can be calculated from the integration of molecular pairwise interactions across the interface. The relation between the work of adhesion (which equals the negative of interfacial energy), surface free energy, and contact angle (θ) can be described by the Young-Dupre equation [36]:

$$\gamma(1+\cos\theta) = W_{ad} = |W(h)| \tag{1}$$

The surface tension of water γ is 0.072 J/m^2. To calculate interfacial energy W, we first consider the generic half-space fluid interacting with half-space substrate (the situation of water on copper and water on graphite). The classic model of wetting assumes that the interaction of two surfaces is the summation of all the molecular pair-wise interactions across the interface. Thus, when the van der Waals interaction is chosen in a 12-6 Lennard-Jones form, the interfacial energy can be expressed as [37]:

$$W(h) = \frac{c}{h^8} - \frac{A}{12\pi h^2} \tag{2}$$

where h is the separation between the surfaces of interest. The Hamaker constant A is taken as $A_{H_2O\text{-}Cu} = 12.2 \times 10^{-20}$ and $A_{H_2O\text{-}graphite} = 9.08 \times 10^{-20}$ J, following the $A_{12} = (A_{11}A_{22})^{1/2}$ mixing rule. Here c denotes the strength of short-range repulsion, which is taken so as to match the contact angles for water on graphite and water on copper obtained from the experiments: $c_{H_2O\text{-}Cu} = 2.52 \times 10^{-80}$ J m^6, $c_{H_2O\text{-}graphite} = 0.98 \times 10^{-80}$ J m^6. The equilibrium separations are found to be ~1.77 Å and ~1.59 Å for water on copper and water on graphite, respectively.

Next, let us consider the situation of water on the copper substrate with graphene in between. The interfacial energy for this case can be expressed as [35]:

$$W(h) = \left(\begin{array}{l} \dfrac{c_{H_2O-graphite}}{h^8} - \dfrac{c_{H_2O-graphite}}{(h+d)^8} + \dfrac{c_{H_2O-Cu}}{(h+d)^8} - \\[2ex] \dfrac{A_{H_2O-graphite}}{12\pi h^2} - \dfrac{A_{H_2O-graphite}}{12\pi(h+d)^2} + \dfrac{A_{H_2O-Cu}}{12\pi(h+d)^2} \end{array} \right) \tag{3}$$

where h is the separation between water and the substrate and d is the thickness of the graphene film. When $d = 0$, Equation (3) reduces to the correct form for work of adhesion for water on Cu substrate. When d approaches infinity, Equation (3) reduces to the correct form for water on graphite. Figure 1.6 shows the prediction using Equation (3) for the water contact angle transition from bulk copper to bulk graphite with increasing numbers of graphene layers on the copper slab. The thickness of one graphene layer is assumed to be ~0.34 nm in the simulations. The wetting angle transition predicted by Equation (3) is consistent with experimental observations. This indicates that the wetting

transparency of graphene is attributable to its extreme thinness. The van der Waals interaction [Equation (3)] is calculated by integrating the interaction of all the molecules in the fluid with all the molecules in the substrate, which, therefore, results in wetting transparency of the ultrathin graphene monolayer to the relatively long-range van der Waals interactions. However, it should be noted that the wetting transparency of graphene breaks down for surfaces such as glass. In spite of its extreme thinness, the presence of graphene at the water-glass interface disrupts the short-range chemical interactions (hydrogen bonding networks), which dictate the water/glass contact angle. Therefore, for surfaces where chemistry plays the dominant role, graphene coatings do not provide wetting transparency.

Due to its extreme thinness, graphene has an unparalleled ability to provide transparency to van der Waals interactions. This is illustrated in Figure 1.6, where the water contact angle transition from copper to graphite is shown for carbon film coatings on copper with thicknesses
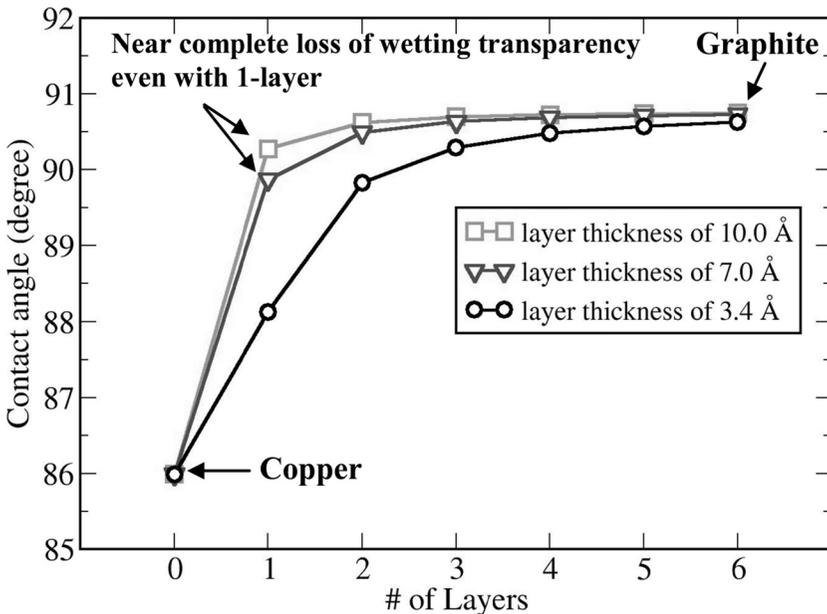
FIGURE 1.6. *Continuum predictions using the classical effective interface potential approach for water contact angle transition from copper to graphite with carbon coating layers of thickness 0.34 nm, 0.7 nm, and 1 nm. As the number of layers is increased, the water contact angle increases from copper and saturates at the bulk graphite value. However, even a single 0.7 nm thick layer fails to show significant wetting transparency effect. This highlights the need for the extreme thinness of graphene (~0.3 nm) in terms of achieving wetting angle transparency. (Adapted from [35] with permission).*

of 0.34 nm, 0.7 nm, and 1 nm using Equation (3). It is clear that even ultrathin 0.7 nm or 1 nm coatings fail to provide wetting transparency. The wetting transparency effect becomes apparent only when the coating thickness is reduced to ~0.34 nm (i.e., thickness of graphene). Sputtered oxide or polymer films cannot rival such extreme levels of thinness. Hexagonal boron nitride (h-BN) is the only known material system that could match graphene's thinness; however, it is very challenging to deposit monolayer h-BN on large area substrates. By contrast, roll-to-roll deposition methods have already been developed [33] to deposit monolayer graphene films several tens of inches in dimensions for flexible electronics.

Graphene also exhibits an extraordinary ability to passivate a surface. Graphene is the ideal impermeable membrane and not even a proton can pass through defect-free graphene. Therefore, conformal coating of graphene on copper prevents the copper from oxidizing [40]. This can have wide-ranging impact in heat-transfer applications, where copper is the material of choice due to its very high thermal conductivity. Copper oxide acts as an interfacial thermal barrier, which significantly degrades heat transfer across copper interfaces. This problem could be overcome by simply coating a monolayer graphene film onto copper.

1.3. SYNTHESIS OF GRAPHENE

There are four basic methods [25] used for graphene synthesis: (1) chemical vapor deposition; (2) epitaxial growth of graphene on electrically insulating substrates; (3) mechanical exfoliation of graphene from bulk graphite (e.g., using Scotch tape); and (4) reduction of graphene derivatives such as graphene oxide. Among these methods (1) and (2) can be broadly classified as bottom-up methods, while methods (3) and (4) are top-down approaches. Among these, reduction of graphene oxide and chemical vapor deposition are the two methods that show the greatest promise for bulk production of graphenes at the scale necessary for composites applications. These two methods are described in brief below.

1.3.1. Reduction of Graphene Oxide

In this approach the starting material used is graphite, which is first converted to graphite oxide using a modified Hummers method [25]. The typical procedure for this is as follows: a reaction flask with a me-

chanical stirrer is charged with sulfuric acid (87.5 ml) and nitric acid (45 ml) and cooled by immersion in an ice-water bath. Fifteen minutes later, graphite flakes (5 g) are introduced into the flask under vigorous stirring to avoid agglomeration. Potassium chlorate (55 g) is then added into the suspension slowly. After reacting for 96 h at room temperature, the suspension is diluted with a mass of deionized water. Graphite oxide precipitate is then washed with HCl solution (10%) to eliminate sulphate ions. Barium chloride can be used to test whether the sulphate ions are eliminated. Once this is confirmed, the graphite oxide is extracted using a high-speed centrifuge and is washed with deionized water until the pH value becomes neutral. After drying in a vacuum oven at ~80°C for ~24 h, the graphite oxide is now ready for use.

It is important to check whether the graphite has been fully oxidized to graphite oxide, as this can have a strong effect on the subsequent exfoliation of graphite oxide into graphene oxide nanosheets. For this, X-ray diffraction (XRD) is a powerful tool. Figure 1.7(a) shows the XRD patterns of natural graphite and graphite oxide. Natural graphite exhibits a strong and sharp peak at 26.5°, indicating a highly ordered structure. The calculated intra-gallery spacing of graphene sheets in graphite structure is ~0.34 nm. This peak disappears after oxidation of the graphite, while a new one arises at 12.3°, corresponding to an intra-gallery spacing of ~0.72 nm, which implies complete oxidation of graphite. The increased spacing arises from the fact that a variety of oxygen moieties including hydroxyl, epoxide, carbonyl, and carboxylic functional groups are attached to the individual graphene sheets due to the oxidation process [25]. The resulting layered structure is called graphite oxide and is composed of graphene oxide sheets (i.e., graphene functionalized with hydroxyl, epoxide, carbonyl, and carboxylic groups). The attachment of the aforementioned oxygen-containing functional groups disrupts the sp^2 bonding network in graphene, creating local sp^3 islands. Graphene oxide is, therefore, electrically insulating compared to its parent graphene.

As Figure 1.7(a) indicates, the physical separation between graphene oxide nanosheets in graphite oxide is ~0.7 nm compared to ~0.34 nm in graphite. The implication of this is that the inter-sheet van der Waals interactions in graphite oxide are significantly weaker in comparison to the original graphite structure. It is, therefore, far easier to exfoliate graphite oxide then it is to exfoliate graphite directly into graphene. There are two basic approaches to exfoliating graphite oxide. The first method involves ultrasonication of graphite oxide in water. Water is

able to penetrate into the inter-layer spacing in graphite oxide because of the strongly hydrophilic nature of the oxygen moieties on graphite oxide. This causes the graphite oxide to exfoliate completely in water to produce a colloidal dispersion of individual graphene oxide nanosheets in water. In the last step, these graphene oxide nanosheets are chemically reduced to graphene in solution using reducing agents such as hydra-
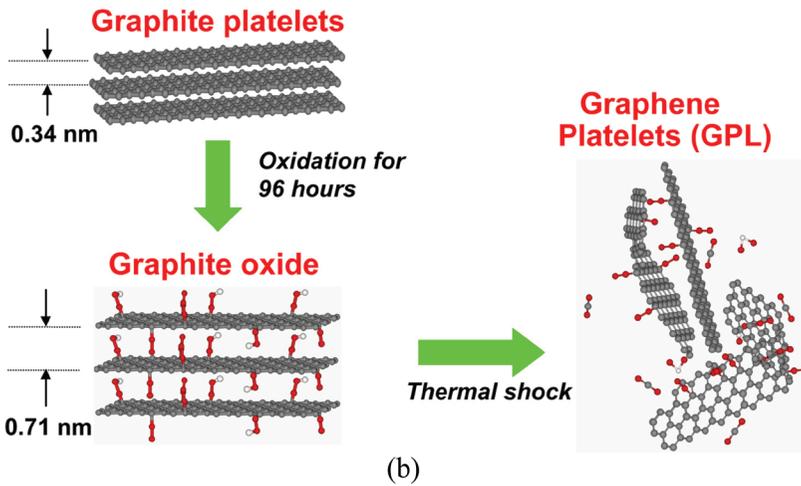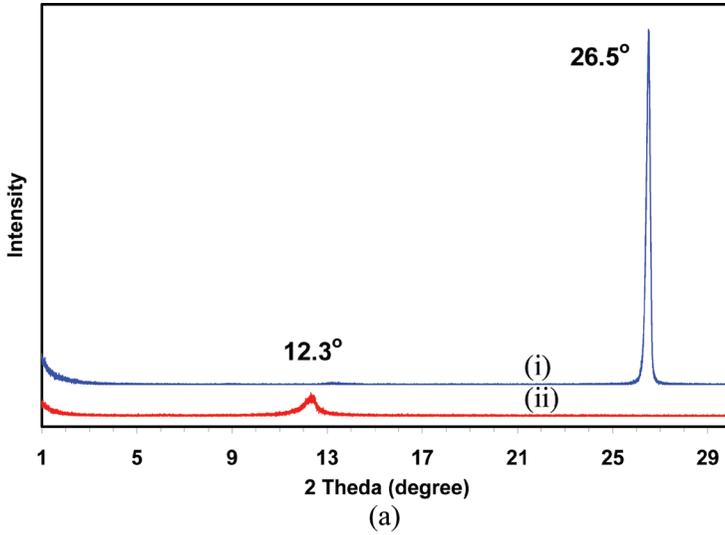

FIGURE 1.7. *(a) X-ray diffraction patterns of natural graphite (i), graphite oxide (ii). (b) Schematic representation of the method used to exfoliate graphite into bulk quantities of graphene platelets. (Adapted from [57–58], with permission).*
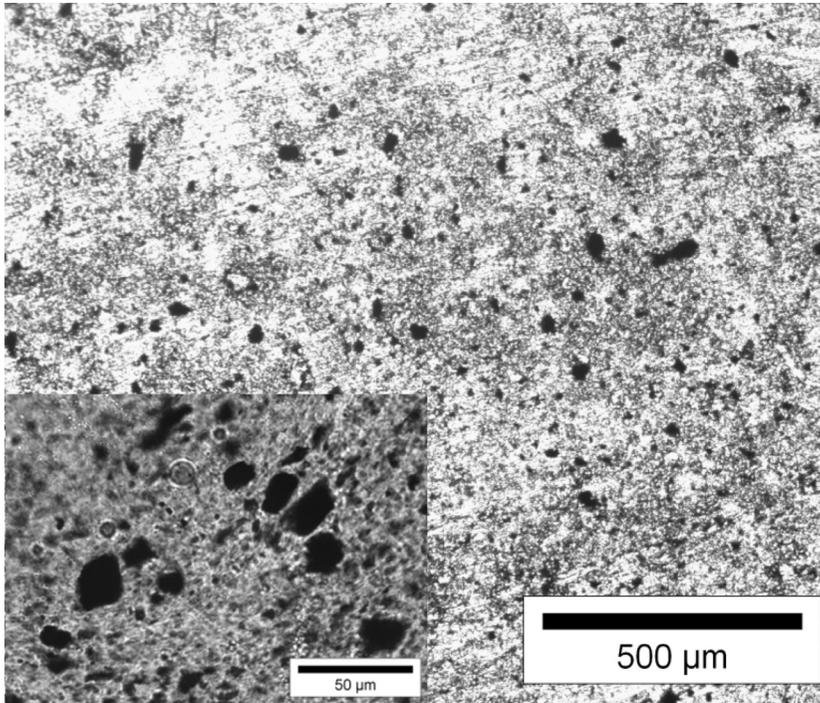
FIGURE 2.4. Optical micrograph showing graphene platelet dispersion in an epoxy. In the inset, the average GPL diameter can be seen to be ~5 µm, scale bar (50 µm).

under transmittance mode. These micrographs can be converted into binary images for image analysis as shown in Figure 2.5(a). Figure 2.5(b) shows the typical plot of average graphene platelet size (diameter) as a function of its weight % for an epoxy polymer. At each GPL weight %, at least 4–5 samples should be imaged to obtain a reliable estimate of the average platelet diameter. It is clear from the plot that there is a sharp increase in the graphene cluster size above a loading fraction of ~0.125%, indicating a significant degradation in dispersion above ~0.125% weight fraction of GPLs.

2.2. TENSILE PROPERTIES: YOUNG'S MODULUS AND ULTIMATE TENSILE STRENGTH

Tensile properties of a material can be determined from stress vs. strain curves obtained by the application of a static load uniformly over the material cross-section. Tensile tests are commonly done to obtain the relevant mechanical properties of a material, such as Young's modu-

(a)

wt. %
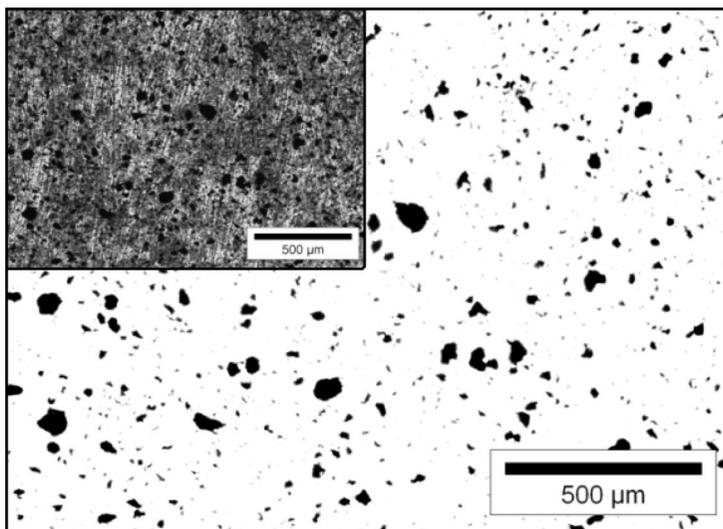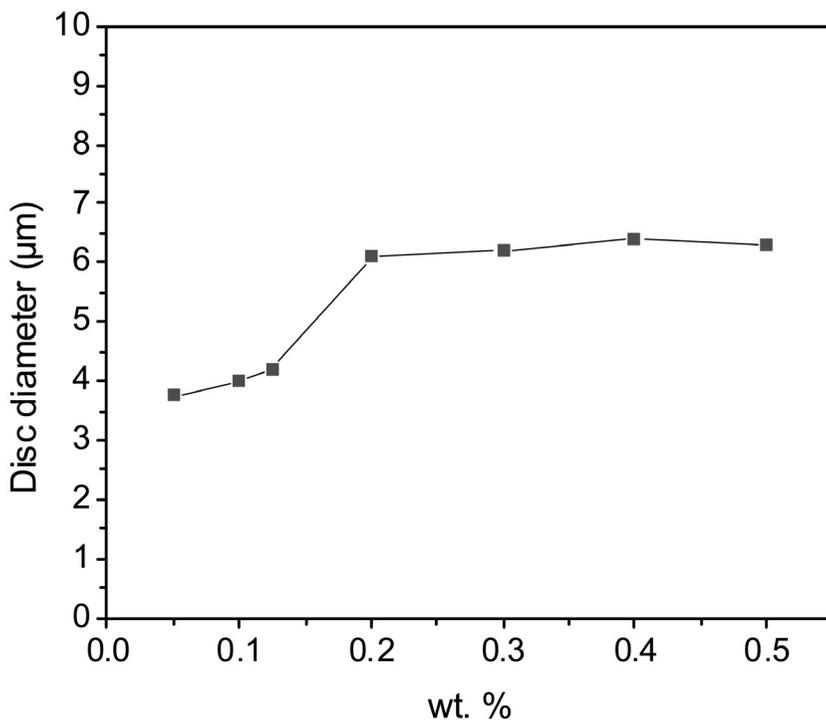
(b)

FIGURE 2.5. *(a) Low magnification binary image of 0.1 weight % of GPL in epoxy; the inset shows the actual optical micrograph. (b) Graphene platelet diameter as a function of its increasing weight % in epoxy.*

35

lus, strain-to-failure, ultimate tensile strength, and toughness (i.e., total energy absorbed prior to failure).

The engineering stress and engineering strain in the material are used to avoid the use of a geometry factor. The engineering stress σ is given by:

$$\sigma = \frac{F}{A} \tag{1}$$

where F is the instantaneous load applied perpendicular to the sample and A is the original cross-sectional area of the sample. The ultimate tensile strength (UTS) is the maximum stress a material can withstand under tensile load. It is given by the maximum stress in the engineering stress-strain curve. The engineering strain σ is given by:

$$\varepsilon = \frac{L - L_o}{L_o} \tag{2}$$

where L is the final sample length and L_o is the original sample length.

Young's modulus measures the ability of a material to resist elastic deformation under applied stress, given by the slope of the stress-strain curve below the yield point. It is given by Hooke's law between σ and ε:

$$E = \frac{\sigma}{\varepsilon} \tag{3}$$

The modulus is a direct measure of microscopic interatomic resistance to stretching. Different materials have different modulus, depending on their interatomic bonding. Polymers have a range of modulus, varying from a few MPa (e.g., Polydimethylsiloxane) up to 3 GPa (e.g., epoxy resins). Compared to polymers, the modulus values for ceramics reside at the other end of the spectrum, varying between a few tens to few hundreds of GPa. The two materials with highest reported Young's modulus are carbon nanotubes and graphene, with values approaching 1 TPa [10].

Various theoretical models in the literature and their modifications complemented with experimental results help predict and estimate the composite modulus as a function of matrix, filler, and interface properties. Some of the models are discussed below.

Iso-stress and Iso-strain model: The composite modulus generally lies between the upper and lower bound of the modulus given by the Iso-strain [Equation (4)] and the Iso-stress [Equation (5)] models [4].

$$E_c = E_f V_f + E_m V_m \tag{4}$$

$$E_c = \frac{E_f E_m}{E_f V_m + E_m V_f} \tag{5}$$

where E_m, E_f and E_c are the elastic modulus of the matrix, filler, and composite, respectively, and V_m and V_f are the volume fractions of matrix and filler. Equations (4) and (5), called the rule of mixture and the inverse rule of mixture, give poor modulus prediction as they assume all the fillers have the same orientation and do not consider imperfect filler-matrix interface properties.

Mori-Tanaka model: The Mori-Tanaka model is used to predict the stiffness tensor of composites under the assumption that the fibers and matrix undergo the same average strain. Derived from the principles of Eshelby's inclusion model for ellipsoidal particles in an infinite matrix, this model gives the best predictions for high aspect ratio fillers, but predicts negligible reinforcement for aspect ratio equal to unity, i.e., particulate fillers. The model [4] effectively takes into account the macroscopic average strain and the fluctuation strain due to the neighboring fibers, giving the stiffness of the composite as:

$$\mathbf{C}^{comp} = \mathbf{C}^m + f_f (\mathbf{C}^f - \mathbf{C}^m)[\mathbf{I} + \mathbf{S}^E (\mathbf{C}^m)^{-1}(\mathbf{C}^f - \mathbf{C}^m)]^{-1} *$$
$$(f_m \mathbf{I} + f_f [\mathbf{I} + \mathbf{S}^E (\mathbf{C}^m)^{-1}(\mathbf{C}^f - \mathbf{C}^m)]^{-1})^{-1} \tag{6}$$

where, $\mathbf{C}^{comp}$, $\mathbf{C}^m$ and $\mathbf{C}^f$ are the stiffness matrices of the composite, matrix, and fiber , respectively; $\mathbf{S}^{comp}$, $\mathbf{S}^m$ and $\mathbf{S}^f$ are the compliance matrices of the composite, matrix, and fiber, respectively; and f_f and f_m are the volume fractions of fiber and matrix in the composite and $\mathbf{I}$ is a unit matrix.

Halpin-Tsai model: Another very useful and practical model for uni-directional and discontinuous-filler composites is the Halpin-Tsai model [11]. The Halpin-Tsai equations are useful for obtaining various composite properties, including modulus, using a parameter ζ, which is a measure of the reinforcement geometry and loading conditions. The modulus of the composite is given by:

$$E_c = E_m \left(\frac{1 + \varsigma \eta V_f}{1 - \eta V_f} \right) \tag{7}$$

$$\eta = \frac{\dfrac{E_f}{E_m} - 1}{\dfrac{E_f}{E_m} + \varsigma} \tag{8}$$

where E_m, E_f and E_c are the elastic modulus of the matrix, filler, and composite, respectively, and V_f is the filler volume fraction. The Halpin-Tsai equation [Equation (7)] has particularly proven very useful for predicting the properties of short-fiber and particulate-reinforced composites. For $\varsigma = 0$ the equation takes the form of the inverse rule of mixture and for $\varsigma = \infty$ it takes the form of the rule of mixture. A shape factor of $2w/t$ (w is filler length, t is filler thickness) is taken for ς [12], which reduces for a spherical particle to $\varsigma = 2$.

As Halpin-Tsai considered only the ideal case of a perfect particle-matrix adhesion, the model was improved by Lewis-Nielsen and Mc-Gee and McCullough [13–14], whose models take into account weak filler-matrix interfaces. The modified composite modulus was given as:

$$E_c = E_m \left\{ \frac{1 + (k_E - 1)\beta V_f}{1 - \beta \mu V_f} \right\} \tag{9}$$

where k_E is the Einstein's coefficient, which determines the degree of filler-matrix adhesion. β takes into account the relative modulus of the filler and the matrix. It is given by:

$$\beta = \frac{\dfrac{E_f}{E_m} - 1}{\dfrac{E_f}{E_m} + (k_E - 1)} \tag{10}$$

and μ is given as:

$$\mu = 1 + \frac{(1 - V_f)}{V_{max}} [V_{max} V_f + (1 - V_{max}) V_m] \tag{11}$$

where V_{max} is calculated from the Nielsen and Landel model [15].

Static tensile tests are typically conducted on dog-bone shaped [Figure 2.6(a)] test coupons following ASTM D638 standard. Figure

2.6(b) shows typical tensile stress vs. tensile strain plots for GPL/epoxy nanocomposites with ~0.1% of GPL additives. For comparison, data is also shown for the same weight % of single-walled carbon nanotubes (SWNTs) and multi-walled carbon nanotubes (MWNTs) in epoxy, as well as the neat (pristine) epoxy matrix. The results of the static tensile tests [16–17] are summarized in Figure 2.7. To check for repeatability of the data, at least four specimens of each nanocomposite at the same filler weight fraction of ~0.1 wt. % were manufactured and tested. The weight fraction of 0.1% was chosen to ensure relatively homogeneous dispersion of fillers. Figure 2.7(a) shows the ultimate tensile strength measurements for the pure epoxy and the nanocomposite samples. Clearly, the GPL additives far outperform the SWNT and MWNT fillers. The tensile strength of the GPL/epoxy nanocomposite (~78 MPa) is

(a)

(b)
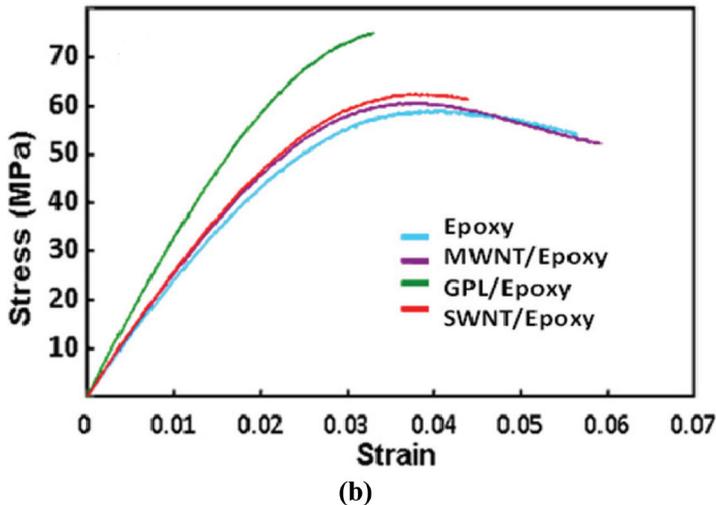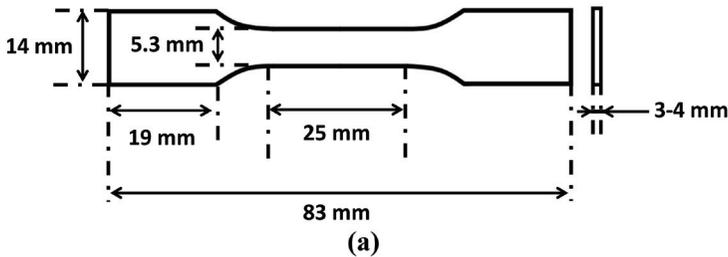
FIGURE 2.6. *(a) Sample geometry for tensile tests. (b) Typical tensile stress vs. tensile strain curves for testing of baseline epoxy and nanocomposites with ~0.1% weight fraction of graphene (GPL), multi-walled carbon nanotube (MWNT), and single-walled carbon nanotube (SWNT) fillers. (Adapted from [16–17] with permission).*
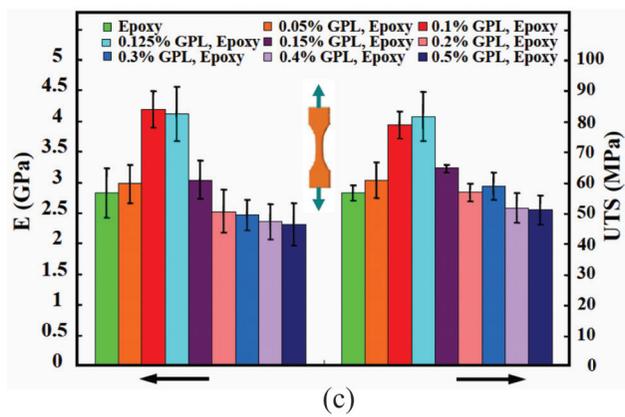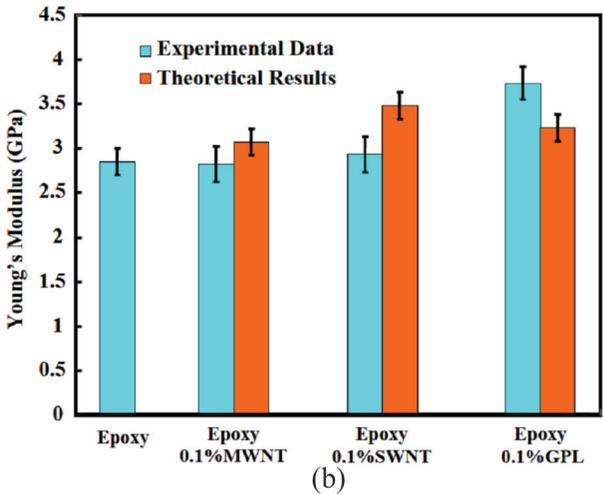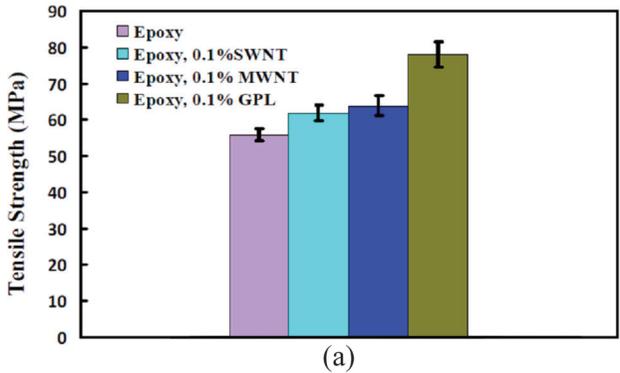
FIGURE 2.7. *(a) Ultimate tensile strength (UTS) for the pure epoxy and nanocomposites. (b) Young's modulus (E) of nanocomposite samples with 0.1 wt. % weight of fillers is compared to the baseline epoxy. Theoretical results computed using the Halpin-Tsai equation for fiber-reinforced composite materials are also shown. (c) Effect of GPL loading fraction on the Young's modulus (E) and ultimate tensile strength (UTS) of the composite structure. (Adapted from [16–17] with permission).*

Hybrid Graphene/Microfiber Composites

GRAPHENE fillers have demonstrated an ability to enhance the mechanical properties of a variety of polymer matrices, as illustrated in Chapter 2 of this book. Significant enhancements in the polymer's stiffness, strength, damping, fracture toughness, and fatigue resistance have been reported. Such nanocomposites can be considered as "two-phase" systems, with the graphene and the polymer chains comprising the two phases in the composite. By contrast, study of "three-phase" composites has not received the same level of attention. The three phases include graphene, the polymer matrix, and conventional microscale continuous fibers (e.g., Kevlar, glass or Graphite fibers). It should be noted that for high performance structural applications (e.g., in the aerospace or automotive industry), a two-phase nanocomposite without continuous microfibers to carry the load appears unlikely to provide sufficient mechanical stiffness or strength to be competitive. Therefore, it is important to investigate three-phase nanocomposites involving the combination of a graphene-modified matrix, together with conventional microfiber reinforcement, and compare its performance to the traditional microfiber-reinforced polymer composites that are used by industry.

Improved mechanical properties of such fiber-reinforced composites (FRCs) can have strong practical applications. FRCs, with their favorable strength-to-weight and stiffness-to-weight ratios, are replacing their metal counterparts in a variety of high performance structural applications [1–2]. However, the principal limitation of FRCs is their brittle failure and insufficient fatigue life, which results in deficiencies in terms of performance, cost, safety, and reliability of structural components [3–4]. Consequently, there is great interest in developing new

concepts for fatigue-resistant FRC composite materials. Wind energy is one of the emerging industries where such new fatigue-resistant materials can have a high impact [5]. Wind turbine blades are typically composed of glass or carbon-fiber epoxy composites and are prone to fatigue failure due to large cyclic bending loads encountered by the blades during regular operation. Wind is the fastest growing energy technology (~$50 billion investment in 2008) on the globe [5] and enhancing the fatigue properties and the operating life of FRC materials used in wind turbine construction is, therefore, of great practical relevance.

The bulk of the material included in this chapter has been adapted from Reference [11], published by the author's group and his collaborators.

3.1. PROCESSING OF HIERARCHICAL GRAPHENE COMPOSITES

Bulk quantities of graphene platelets (GPLs) are necessary for the processing of such hierarchical FRC composites. A convenient method to mass-produce such GPLs is by the one-step thermal reduction and exfoliation of graphite oxide [6–10]. This method has been discussed in detail in Chapter 1. In this section, I will demonstrate how such graphene platelets can be combined with traditional E-glass fabric plies (bi-directional, twill weave, style 7725 from Fibreglast, USA) and a Bisphenol-A based epoxy matrix (Epoxy 2000 from Fibreglast, USA) to generate hybrid or hierarchical FRC nanocomposites. The first step in the fabrication of these composites is to disperse the as-produced GPLs in the thermosetting epoxy resin via ultra-sonication. This method has been discussed in detail in Chapter 2. Then, the GPL/epoxy blend is painted, layer-by-layer, on the glass-fibers. At least eight glass-fiber plies are typically used to construct the composite laminate. For smaller number of plies, the test results may not be representative of bulk laminates. After all the glass-fiber plies are laid up and wetted with the GPL-infused epoxy, a vacuum bag is placed over the system, and the sample is allowed to cure under vacuum for 24 hours at room temperature. During this process, excess epoxy is extracted out of the composite into an absorbent cloth inside the vacuum bag. Lastly, the composite is taken out of the vacuum bag and placed in an oven at 90°C for high temperature cure for four hours. By this method, the estimated volume fraction of the glass micro-fibers in the composite structure typically lies in the 0.6 to 0.8 range.

Figure 3.1(b) illustrates the structure [11] of the hybrid composite. Scanning electron microscopy (SEM) imaging showing the hierarchi-
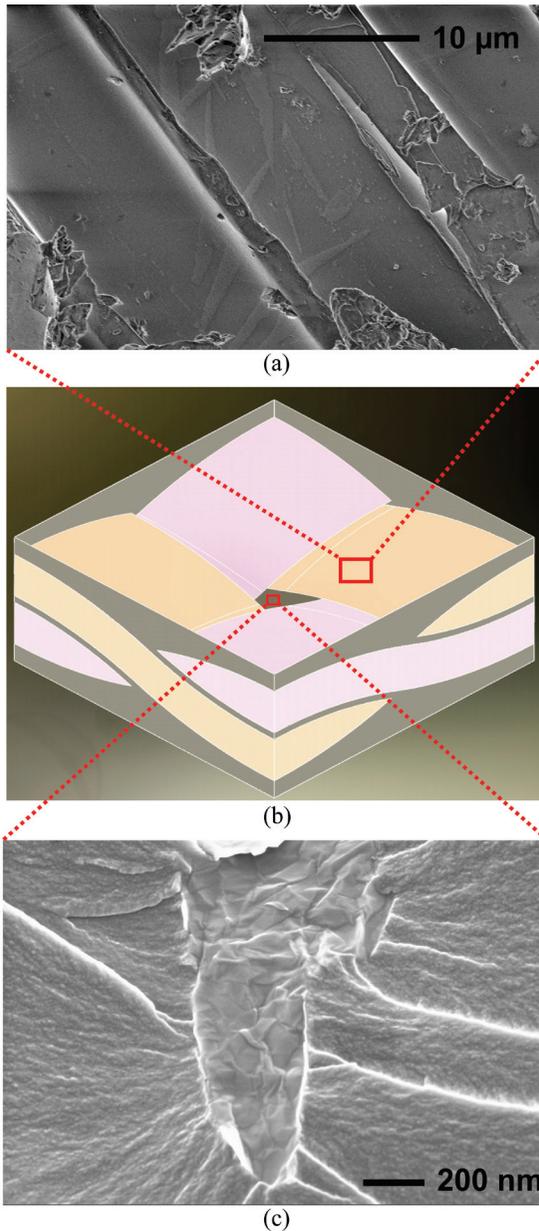
FIGURE 3.1. *Schematic representation of the unit cell that constitutes the 3-phase hierarchical composite. The three phases include interwoven E-glass strands laid up in the 0–90 direction, the epoxy matrix that serves as the binder, and GPLs dispersed into the epoxy matrix. Top scanning electron microscopy (SEM) image shows individual microscale glass fibers within the woven fabric strand. GPL additives interlinking the glass fibers through the epoxy matrix are also discernable. Lower SEM image shows a typical GPL/epoxy-matrix interface obtained from the matrix-rich region of the composite; there is no indication of interfacial debonding, which suggests a strong interface. (With permission from [11]).*

cal structure of the composite with the three main phases (i.e., the E-glass fibers, the epoxy resin, and the graphene platelets interlinking (or interlacing) the glass fibers) is seen in Figure 3.1(a). Figure 3.1(c) is a typical SEM image of the sample's fracture surface, indicating a graphene platelet embedded in the epoxy matrix. Although the sample was mechanically fractured, the integrity of the GPL/epoxy interface is maintained with no sign of debonding, suggesting a strong interface.

3.2. TESTING OF HIERARCHICAL GRAPHENE COMPOSITES

In a two-phase composite material, graphene is shown to enhance a broad range of mechanical properties of the host polymer matrix, such as Young's modulus, ultimate tensile strength, fracture toughness, fatigue crack propagation resistance, creep resistance, and wear resistance [12–18]. For a hierarchical three-phase composite with microfibers, the situation is not the same. Along the microfiber direction (i.e., laminate in-plane direction), the reinforcing ability of the distributed graphene platelets is negligible compared to the continuous microfibers that run along the length of the structure. In-plane laminate properties, such as Young's modulus and ultimate tensile strength, remain nearly identical despite the presence of graphene in the epoxy matrix. There is some improvement when one considers out of plane static mechanical properties, such as flexural bending stiffness and flexural strength. There is a ~20–30% increase in flexural strength (Figure 3.2), while the flexural modulus remained unchanged for the hierarchical and baseline composites. However, the situation changes dramatically when one considers the fatigue properties of the composite.

Fatigue test data on the hierarchical glass-fiber/epoxy/GPL laminates in a 3-point bend test configuration [11] can be generated as shown schematically in the inset of Figure 3.3. For the test data presented in this chapter, the cyclic loading tests were performed at a frequency of ~5 Hz and the stress ratio (R: minimum-to-maximum applied stress) was 0.1. Figure 3.3 shows the maximum flexural bending stress (S) vs. the number of cycles to failure (N) for the hierarchical composite for various GPL weight fractions up to a maximum of 0.2%. Note that 0.2% is the weight fraction of GPL in the epoxy resin. The weight fraction of GPLs in the entire laminate (including the E-glass microfibers) was estimated to be an order of magnitude lower (~0.02% for ~0.2% weight of GPLs in the epoxy). At each stress level, a minimum of three

samples with the same GPL loading were tested to failure and the averaged results are represented as S-N curves (Figure 3.3). The results indicate a significant increase in the number of cycles to failure across the entire range of applied stresses. Increasing the GPL weight fraction from 0.05 to 0.2% had a strong beneficial impact on the fatigue life enhancement. At a stress level of ~500 MPa, the fatigue life of the composite with ~0.2% by weight of GPLs in the epoxy resin is enhanced by ~1200-fold as compared to the baseline glass-fiber/epoxy composite without the GPLs. At lower stress levels (< 400 MPa), about two orders of magnitude increase in fatigue life of the hierarchical composite relative to the baseline can be seen.

Figure 3.4 compares the performance of GPLs with SWNT and MWNT reinforcement at a constant nanofiller weight fraction of ~0.2%. The processing conditions used for SWNT and MWNT composites were identical to that of graphene. Depending on the applied stress, GPLs offer a 1–2 orders of magnitude increase in fatigue life as compared to MWNTs and SWNTs at the same weight fraction of additives. Figures 3.3–3.4 show flexural bending fatigue life results. Fatigue tests on hierarchical composites in the uniaxial tensile mode
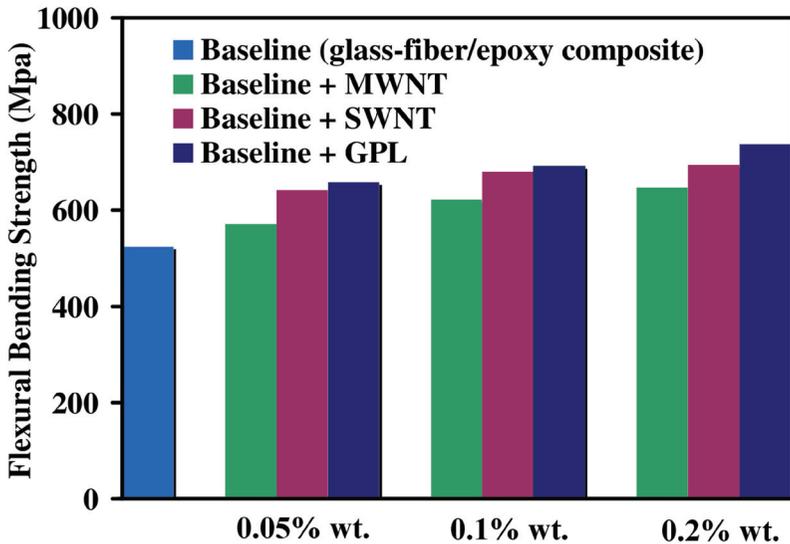
FIGURE 3.2. *Test data for the static flexural bending strength for baseline and hierarchical composites with various weight fractions of SWNT, MWNT, and GPL additives. GPLs were found to perform better than SWNTs and MWNTs at the same loading fraction of additives. For the case of GPL fillers, between 20–30% increase in the flexural strength for the hierarchical nanocomposite over the baseline fiberglass/epoxy composite can be observed. Also, SWNTs are observed to perform better than MWNT fillers.*
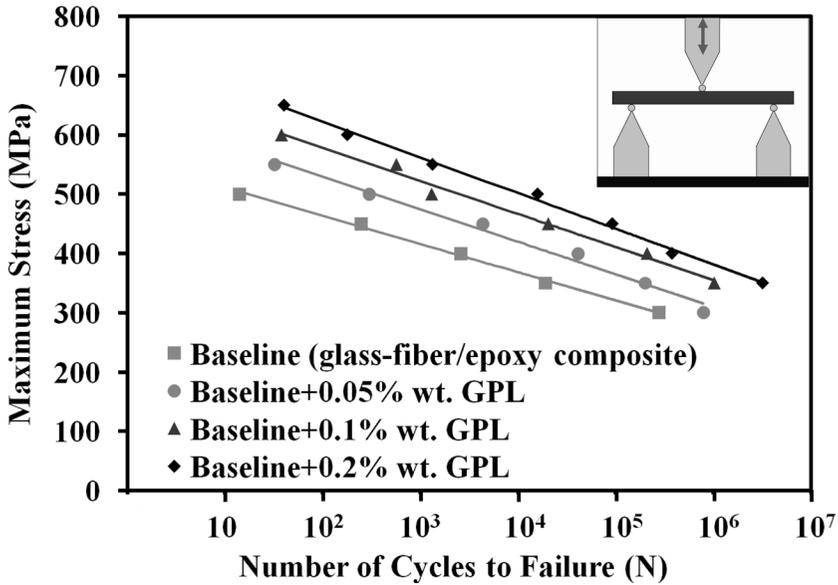
FIGURE 3.3. *Fatigue test results in flexural bending mode. Maximum bending stress (S) vs. number of cycles to failure (N) for baseline glass-fiber/epoxy composites and glass-fiber/epoxy/GPL composites with various weight fractions of GPLs in the epoxy resin. The test is performed in the flexural bending mode as indicated in the inset schematic. (With permission from [11]).*
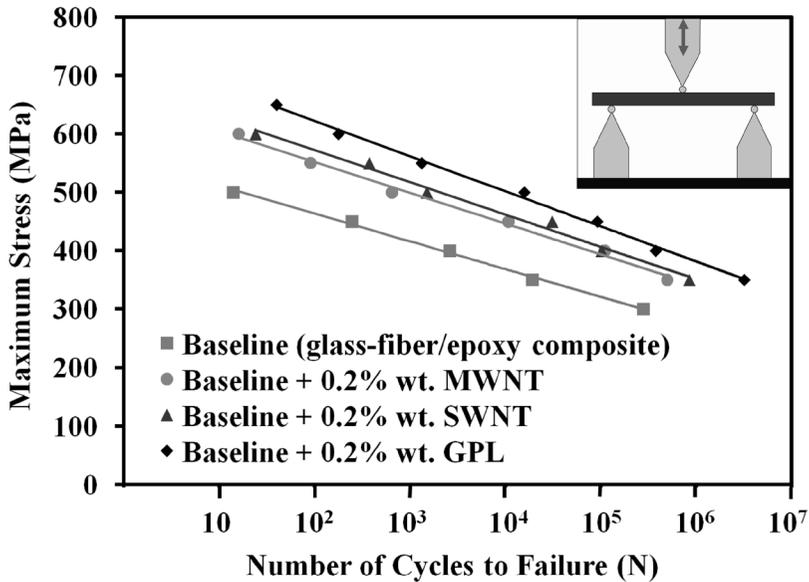
FIGURE 3.4. *Fatigue test results in flexural bending mode. S-N curve comparing the fatigue response in flexural bending mode of GPLs with SWNT and MWNT additives at the same weight fraction of ~0.2% of the epoxy resin weight. (With permission from [11]).*

Index